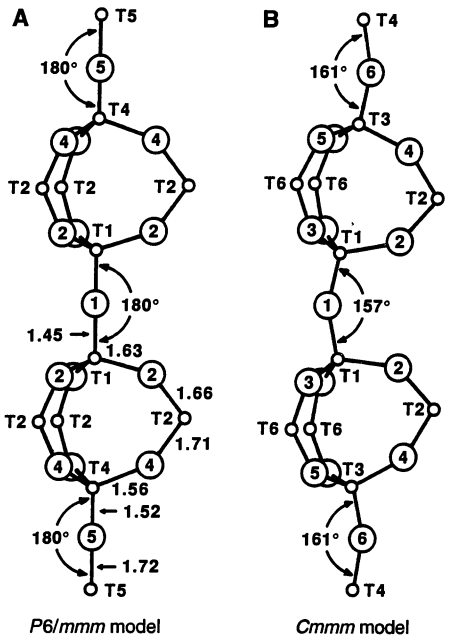

Fig. 5. Dimeric chain of T-O-[4³]-O-[4³]-O-T in MCM-22. (**A**) Bond lengths and angles derived from the Rietveld refinement in space group *P6/mmm*. (**B**) Bond angles derived from the DLS refinement in space group *Cmmm*.

agreement with observed XRD data that was obtained with this model. Despite its unusual topology, the framework connectivity for MCM-22 proposed here yields the best agreement with observed data. The discrepancy indices for the refinement are not unreasonable and are comparable with those (9) of other framework materials determined from powder XRD data.

The structure of MCM-22 may allow for a variety of applications in the petrochemical and refining industries. For example, MCM-22 may find applications in the catalysis of carbenium ion–mediated reactions, particularly those where the reactant size or the structure of the transition state intermediate is affected by the steric constraints presented by this zeolite.

REFERENCES AND NOTES

1. M. K. Rubin and P. Chu, U.S. patent 4,954,325 (1990) (assignee: Mobil Oil Corporation).
2. The chemical composition (in weight percent) of this product was determined to be N, 1.67; Na, 1.0; B, 1.06; Al_2O_3, 0.37; and SiO_2, 76.5. The molar ratios were SiO_2/Al_2O_3, 351; SiO_2/B_2O_3, 26.0; and $SiO_2/(Al+B)_2O_3$, 24.2.
3. A portion of the calcined, hydrated sample was placed in a flat plate and bathed in an 8 mm by 1 mm beam of 1.5371 Å radiation. A Si(111) single-reflection incident-beam monochromator and a Ge(220) analyzer crystal were used. The sample was scanned from $2\theta = 3°$ to 75° in steps of 0.02° with a count time of 8 s per step. The instrument design at X7A uses a nonfocusing diffractometer geometry, so the ω-angle could be rocked during the data collection to reduce preferred-orientation effects that might be present in the sample.
4. Precise values for the unit cell parameters of the calcined material were determined during the Rietveld refinement of the structure. The numbers in parentheses correspond to the standard error in the last digits.
5. Ch. Baerlocher, A. Hepp, W. M. Meier, DLS-76: A Program for the Simulation of Crystal Structures by Geometric Refinement (Institute of Crystallography and Petrography, ETH, Zurich, Switzerland, 1978).
6. Trial models for the MCM-22 framework were constructed with structural fragments deduced from *hk*0 and *h*0*l* HREM lattice images (*10*). These fragments were interconnected to form frameworks satisfying the requirements of tetrahedral network bonding and the crystal symmetry of MCM-22, as determined from ED patterns and the indexing of the experimental XRD pattern. Calculated XRD patterns (*11*) for the models were computed from DLS-refined (*5, 12*) atomic coordinates. The framework model whose computed XRD powder pattern corresponded most closely to the experimental pattern has a maximum topological symmetry of *P6/mmm* (D^1_{6h}, no. 191) (*13*). This model, which produced very low DLS figures-of-merit (*14*) $R = 0.0020$ and $\sigma = 0.0083$, served as the starting point for least squares refinements of the framework versus the experimentally observed XRD pattern by means of the Rietveld procedure (*15*), as implemented in the Generalized Structure Analysis System (GSAS) computer program package (*16*) from Los Alamos National Laboratory. Because of the complexity of the MCM-22 structure and the limited extent of diffracted intensities in the XRD pattern, soft constraints were imposed on interatomic distances during the structure refinement. In particular, T–O distances were specified as 1.61 Å and O–O distances were set to 2.63 Å, in line with idealized silicate geometry about the tetrahedral centers. Distances between adjacent tetrahedral centers were not constrained. Preliminary Rietveld refinement of the DLS-optimized framework with the synchrotron data reduced the discrepancy index R_p to ~0.30 after adjustment of the scale, profile, and lattice parameters. A difference Fourier synthesis computed at this point revealed the presence of nonframework atoms in the structure. Addition of these atoms to the calculated powder pattern and refinement of the soft-constrained framework coordinates resulted in a converged refinement with discrepancy indices $R_p = 0.16$, $R_{wp} = 0.19$, and $R(F^2) = 0.13$. Sixty independent parameters were varied in the refinement, including 46 atom coordinates; 517 reflections were used, along with 76 soft constraints.
7. H. Gerke and H. Gies, *Z. Kristallogr.* **166**, 11 (1984).
8. A cage may be described by the rings of (Si,B)–O from which it is constructed, that is the number of T atoms (*A, B, C, . . .*) in each ring and the total number of each type of ring (*u, v, w, . . .*). This description may be represented by the symbol $[A^uB^vC^w \ldots]$. For example, $[4^25^810^2]$ describes a cage consisting of two 4-rings (rings of 4 T atoms), eight 5-rings, and two 10-rings.
9. L. McCusker, *J. Appl. Crystallogr.* **21**, 305 (1988); E. B. Keller, W. M. Meier, R. M. Kirchner, *Solid State Ionics* **43**, 93 (1990); J. M. Bennett and R. M. Kirchner, *Zeolites* **11**, 502 (1991).
10. Images obtained on a Jeol 4000EX transmission electron microscope (TEM) at the high-resolution electron microscopy facility in the Center for Solid State Science at Arizona State University. The instrument was operated at 400 kV with a top-entry goniometer and has an interpretable resolution of ~1.6 Å at Scherzer defocus. Samples were prepared for study in the TEM by ultramicrotomy.
11. POWD10; D. K. Smith, M. C. Nichols, M. E. Zolensky, College of Earth and Mineral Sciences, Pennsylvania State University, University Park, PA (March 1983).
12. In these refinements, the prescribed T–O, O···O, and T···T distances (where T is a tetrahedrally coordinated atom, either Si or B in this case) were optimized at 1.61, 2.63, and 3.07 Å, respectively, with relative weights of 2.0, 1.0, and 0.1. The lattice parameters were allowed to refine. Both *R* and σ have been defined elsewhere (*17*). According to Gramlich-Meier, DLS refinements that are based on the weighting scheme used here and that produce residuals (*R*) less than 0.003 can be considered as realistic models (*14*).
13. T. Hahn, Ed., *Space-Group Symmetry*, vol. A of International Tables for Crystallography (Reidel, Dordrecht, 1983).
14. R. Gramlich-Meier, *Z. Kristallogr.* **177**, 237 (1986).
15. H. M. Rietveld, *J. Appl. Crystallogr.* **2**, 65 (1969).
16. A. C. Larson and R. B. Von Dreele, GSAS, Generalized Structure Analysis System (MS-H805, Los Alamos Neutron Scattering Center, Los Alamos National Laboratory, Los Alamos, NM, 1988).
17. S. L. Lawton and W. J. Rohrbaugh, *Science* **247**, 1319 (1990).

18. We thank P. A. Labun for technical assistance in obtaining the high-resolution electron micrographs.

11 March 1994; accepted 10 May 1994

Time-Resolved Imaging of Translucent Droplets in Highly Scattering Turbid Media

R. R. Alfano,* X. Liang, L. Wang, P. P. Ho

The spatial distribution of small translucent droplets inside a 50-millimeter-thick Intralipid solution was imaged with a picosecond time and spatial-gated Kerr-Fourier imaging system at a signal level of about 10^{-10} of the incident illumination intensity.

Early ballistic and snake light imaging (*1–9*) offers a nondestructive and noninvasive method to observe translucent objects inside a highly scattering environment. With recent advances in the development of ultrafast lasers and ultrasensitive photodetectors, submillimeter spatial resolution of optical images has been achieved from both opaque (*1, 3, 4*) and translucent (*8–10*) phantoms in modeled turbid media. We report on two-dimensional imaging of translucent droplets; that is, we resolved phantoms without container boundaries and with different

Institute for Ultrafast Spectroscopy and Lasers, Mediphotonics Laboratory, New York State Center of Advanced Technology for Ultrafast Photonic Materials & Applications, Departments of Physics and Electrical Engineering, The City College and The Graduate School of The City University of New York, New York, NY 10031, USA.

*To whom correspondence should be addressed.

densities entering into a highly scattering host Intralipid solution (Kabi Pharmacia, Layton, North Carolina) using time-resolved Kerr-Fourier (KF) imaging. The spatial distribution of the translucent droplets inside the 50-mm-thick scattering host environment can be clearly visualized.

The experimental setup of the time and 4F-space–gated KF transillumination imaging system has been described elsewhere (*3*, *11*). In this 4F system, the transmitted shadow signal located at the front focal point plane was collected and transformed by a lens, L_1, to the Kerr cell located at the back focal plane. With the time and induced spatial gating, the Fourier spectrum after the Kerr cell was retransformed and imaged by the second lens, L_2, to the detector plane. A single shot, Nd^+-glass mode–locked laser that generates 1054-nm, 8-ps pulses was used as the probe. The Kerr gate consisted of a pair of crossed calcite polarizers and a CS_2 cell. The Kerr cell was placed at the back focal plane of the entrance lens. The second harmonic, 527-nm beam was used to actuate the Kerr gate. Higher spatial frequency components from diffusive noise were removed at the Fourier plane by the induced Kerr aperture. A cooled charge-coupled device camera system with 16-bit resolution was used to detect the shadow of the transmitted signal with 2.5×10^5 detection pixels. A Fourier spatial filtering technique coupled with the ultrafast time-gated imaging has greatly improved the dynamic range and the signal-to-noise ratio. The spatial dimension of the gating laser pulse radial profile automatically induces a spatial aperture at the Kerr cell to remove the higher spatial frequencies effectively.

A schematic of the sample phantom and host cell arrangement is shown in Fig. 1. Diluted Intralipid solutions (*10*–*13*) of various concentrations and pure water were used for the phantom droplets in a 2% diluted Intralipid host turbid cell. The inside dimension of the host cell was 50 by 50 by 50 mm. The phantom droplets were generated in a 50-ml Kimex (Baxter Diagnostic, Edison, New Jersey) burette with a straight bore stopcock with a polytetrafluoroethylene plug. The subdivision or the limit of error of this burette is 0.1-ml. For a 2% diluted Intralipid stock solution of 10% (the final solution was 0.2%), the measured attenuation coefficient (*10*) from the KF imaging system of this 2% diluted Intralipid solution is 1/2.6 mm. Because of the additional time-gating, this attenuation coefficient that was measured from the time-spatial–gated approach was found to be larger than the scattering coefficient of ~1/3.7 mm obtained from both the continuous-wave Fourier (*10*) and the standard continuous-wave collimated transmission (*14*) approach. The absolute signal collected was $\sim 10^{-10}$ of the input probe beam. The absorption length of the modeled Intralipid solution is on the order of 500 mm and can be neglected in our experimental arrangements.

Two measured time-resolved KF two-dimensional images of water droplets in the

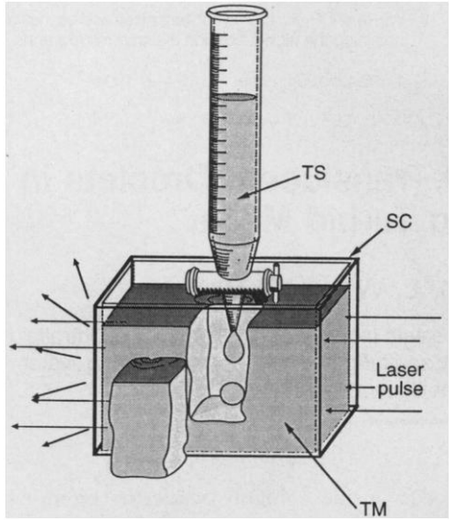

Fig. 1. Experimental arrangement of turbid sample cell and translucent Intralipid phantom droplets. The cut from the side section of the cell displays pictorially the droplet releasing inside the host medium. Abbreviations: SC, sample cell with inside dimensions of 50 by 50 by 50 mm; TM, 2% dilution of a 10% stock Intralipid solution for the host turbid medium; TS, translucent phantom sample, *x*% diluted Intralipid solution in a burette.

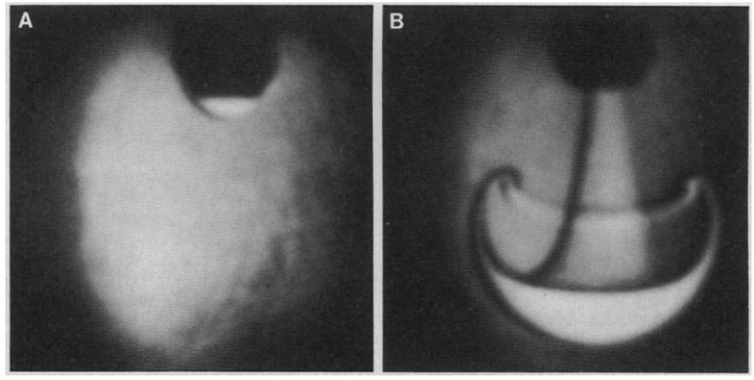

Fig. 2. Early time two-dimensional shadow images of water phantom droplets in a host 50 mm thick of 2% diluted Intralipid stock solution. The spatial distribution of the water drop depends on the amount of water and the delay of release time. The dark shadow at the top middle part of the white laser beam circle is the end tip of the burette. (**A**) Delay of ~2 s from release of the stopper and (**B**) delay of ~10 s from release of the stopper.

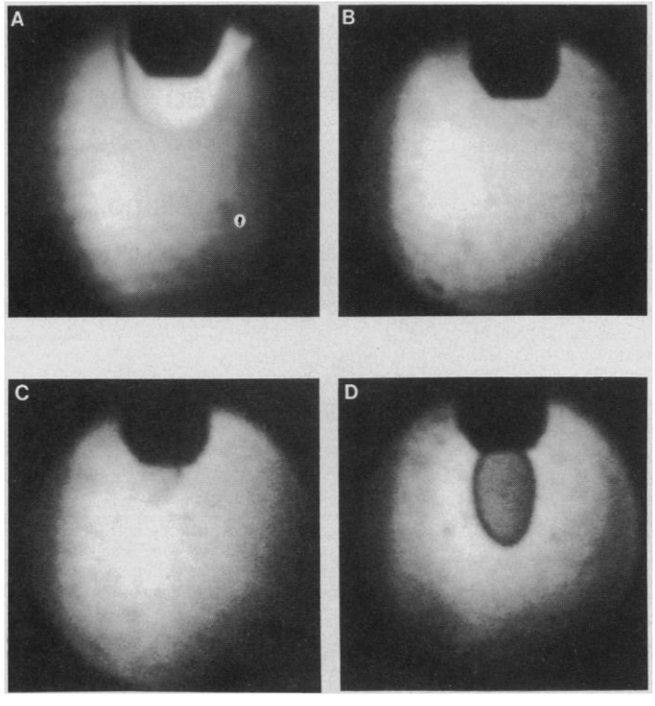

Fig. 3. Early time images of translucent Intralipid phantom drops of various concentrations in a host 50 mm thick of 2% diluted Intralipid stock solution. The images show diluted Intralipid phantom drops at (**A**) 1%, (**B**) 2%, (**C**) 3%, and (**D**) 5% concentrations.

middle of a 50-mm-thick host cell are shown in Fig. 2, A and B. Because the scattering loss from the water droplet is less than that from the surrounding host, the intensity of the projected image of the water droplet was brighter than that of the host. The shape of these water droplets depends on the amount of water released. The delay time between the stopper opening and the photographic time was varied from ~2 to 10 s. The inhomogeneity of the brighter circle in Fig. 2 that corresponds to the collection aperture or signal beam diameter of ~12.7 mm was accounted for by the nonuniformity of the laser intensity distribution.

To determine the contrast of the transmitted early snake light images as shown in Fig. 3, four different phantom droplets with 1, 2, 3, and 5% diluted Intralipid solutions were dropped into a 2% host medium. The projected image from the 5% Intralipid droplet shown in Fig. 3D is the darkest because of the increased scattering from the droplet, while the projected image from the 2% Intralipid droplet shown in Fig. 3B is hardly distinguishable from the surrounding host with the identical scattering property. The image obtained from the 1% Intralipid droplet (Fig. 3A) is brighter and the image from the 3% Intralipid droplet in Fig. 3C is darker than that from the 2% surrounding host. A 1% concentration dilution difference between the phantom droplet and the host medium can be distinguished visually. The changes of the shape of the drop can be measured. A much smaller concentration difference of 0.1% between the phantom droplets and the host medium could be identified with digital video signal processing (*10*). This work demonstrates that small differences in scattering properties and the shapes of small dimension translucent droplets can be spatially determined inside a large host turbid medium that may be useful in moving toward the optical mammography. A droplet phantom inside a scattering host without an artificial container boundary is an ideal object to simulate, for example, a tumor embedded in a tissue or droplets in jet exhaust. Furthermore, the early light transillumination technique can be adapted to determine the spatial distribution of the particle size and shape of the fuel spray in air from a jet nozzle to improve efficient engine design.

REFERENCES AND NOTES

1. L. Wang, P. P. Ho, C. Liu, G. Zhang, R. R. Alfano, *Science* **253**, 769 (1991).
2. M. A. Duguay and A. T. Mattick, *Appl. Opt.* **10**, 2162 (1971).
3. L. Wang, P. Ho, X. Liang, H. Dai, R. Alfano, *Opt. Lett.* **18**, 241 (1993).
4. M. Hee, D. Huang, E. Swanson, J. Fujimoto, *ibid.*, p. 950.
5. D. A. Benaron and D. K. Stevenson, *Science* **259**, 1463 (1993).
6. H. Chen *et al.*, *Opt. Lett.* **16**, 487 (1991).
7. M. Duncan, R. Mahon, L. Tankersley, J. Reintjes, *ibid.*, p. 1868.
8. B. Das, K. Yoo, R. Alfano, *ibid.* **18**, 1092 (1993).
9. K. M. Yoo, B. B. Das, R. Alfano, *ibid.* **17**, 958 (1992).
10. X. Liang, L. Wang, P. Ho, R. Alfano, in preparation.
11. L. Wang, P. Ho, R. Alfano, *Appl. Opt.* **32**, 5043 (1993).
12. M. S. Patterson, B. Chance, B. C. Wilson, *ibid.* **28**, 2331 (1989).
13. F. Liu, K. M. Yoo, R. R. Alfano, *Opt. Lett.* **18**, 432 (1993).
14. H. van Staveren, C. Moes, J. van Marle, S. Prahl, M. van Gemert, *Appl. Opt.* **30**, 4507 (1991).

15. Supported by grants from Mediscience Technology Corporation and the New York State Science and Technology Foundation.

8 February 1994; accepted 12 May 1994

The X-ray Surface Forces Apparatus: Structure of a Thin Smectic Liquid Crystal Film Under Confinement

Stefan H. J. Idziak, Cyrus R. Safinya, Robert S. Hill, Keith E. Kraiser, Marina Ruths, Heidi E. Warriner, Suzi Steinberg, Keng S. Liang, Jacob N. Israelachvili

An x-ray surface forces apparatus for simultaneously measuring forces and structures of confined complex fluids under static and flow conditions is described. This apparatus, combined with an intense synchrotron x-ray source, allows investigation of molecular orientations within a thin liquid crystal film confined between two shearing mica surfaces 3900 angstroms apart. The layer-forming smectic liquid crystal 8CB (4-cyano-4′-octylbiphenyl) adopted a series of distinct planar layer orientations, including the bulk flow-forbidden *b* orientation.

Confinement of complex fluids between two surfaces or in narrow pores is known to strongly alter the collective structure of the trapped molecules in molecular aggregates such as polymers, vesicles, biomembranes, or colloidal particles suspended in the liquid (*1–6*). Molecular dynamics simulations (*7*) indicate that increasing confinement may change the density and positional order, in addition to the molecular orientational order of molecules and aggregates, especially as the decreasing gap size approaches an inherent length scale, such as the diameter of suspended colloidal particles or the radius of gyration of dissolved polymer coils, or ultimately, the diameter of the trapped solvent molecules themselves.

Structural rearrangements within complex fluid systems may also be induced by flow (*8–13*), but such flow-induced effects do not require confinement and occur throughout the bulk fluid, for example, when bulk nematic (*10*) or smectic (*11*) liquid crystals are sheared (Fig. 1). Another important difference between confinement-induced and flow-induced effects is that the former produce equilibrium whereas the latter produce nonequilibrium structures.

The effects of confinement on molecular conformations and transport, as well as the phase behavior of liquids in small pores

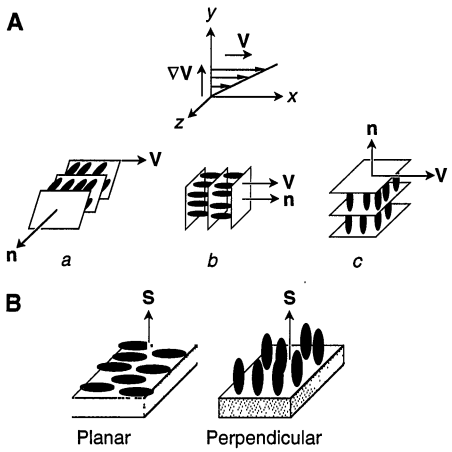

Fig. 1. (**A**) Definitions of the real space layer orientations during flow, following the notation of Miecowicz (*23*): (*a*) The layer normal **n** is along the **z** direction; (*b*) the layer normal is along the velocity **v** direction; (*c*) the layer normal is along the velocity gradient (∇**v**) direction. In orientations *a* and *c*, the velocity is in the plane of the layers. (**B**) Planar and perpendicular (homeotropic) orientations for the liquid crystal molecules at the solid interface.

S. H. J. Idziak and K. E. Kraiser, Materials Department and the Materials Research Laboratory, University of California, Santa Barbara, CA 93106, USA.
C. R. Safinya and H. E. Warriner, Physics Department, Materials Department, and the Material Research Laboratory, University of California, Santa Barbara, CA 93106, USA.
R. S. Hill and S. Steinberg, Department of Chemical Engineering, University of California, Santa Barbara, CA 93106, USA.
M. Ruths, Chemistry Department, University of California, Santa Barbara, CA 93106, USA.
K. S. Liang, Exxon Research and Engineering Company, Annandale, NJ 08801, USA.
J. N. Israelachvili, Department of Chemical Engineering, Materials Department, and the Materials Research Laboratory, University of California, Santa Barbara, CA 93106, USA.